Graphene Structures at an Extreme Degree of Buckling

Youdong Mao,[*,†] **Wei L. Wang,**[‡,∥] **Dongguang Wei,**[§,∥] **Efthimios Kaxiras,**[‡] **and Joseph G. Sodroski**[*,†,⊥]

[†]Dana-Farber Cancer Institute, Department of Pathology, Harvard Medical School, Boston, Massachusetts 02115, United States, [‡]Department of Physics, School of Engineering and Applied Sciences, Harvard University, Cambridge, Massachusetts 02138, United States, [§]Carl Zeiss NTS, LLC, One Corporation Way, Peabody, Massachusetts 01960, United States, and [⊥]Department of Immunology and Infectious Disease, Harvard School of Public Health, Boston, Massachusetts 02115, United States. [∥]These authors contributed equally to this work.

ABSTRACT The distinctive properties of graphene sheets may be significantly influenced by the presence of corrugation structures. Our understanding of these graphene structures has been limited to the mesoscopic scale. Here we characterize angstrom-scale periodic buckling structures in free-standing graphene bilayers produced by liquid-phase processing in the absence of specific substrates. Monochromated, aberration-corrected transmission electron microscopy with sub-angstrom resolution revealed that the unit structures in the major buckling direction consist of only two and three unit cells of graphene's honeycomb lattice, resulting in buckling wavelengths of 3.6 ± 0.5 and 6.4 ± 0.8 Å, respectively. The buckling shows a strong preference of chiral direction and spontaneously chooses the orientation of the lowest deformation energy, governed by simple geometry rules agreeing with Euler buckling theory. Unexpectedly, the overall buckled structures demonstrate geometric complexity with cascaded features. First-principles calculations suggest that significant anisotropic changes in the electronic structure of graphene are induced by the buckling.

KEYWORDS: graphene · aberration-corrected transmission electron microscopy · Euler buckling instability · electronic structure · density functional theory

Graphene, a two-dimensional (2D) carbon crystal, has elicited widespread scientific interest.[1−5] The physical properties of graphene may be significantly influenced by the presence of corrugations.[6−15] Periodic ripples represent an especially desirable means to tailor graphene's properties owing to their controllability.[15−18] The formation of all known periodic ripples, whose wavelengths range from 2 nm to 5 μm, is highly dependent on the use of specific substrates.[16−19] It is unknown whether graphene can endure an extreme degree of buckling on the angstrom scale and how graphene reorganizes its structure in response to conditions that promote such buckling in the absence of specific substrates. Experimental and theoretical studies of these problems would provide insight into the general properties of 2D atomic crystals.

The direct, unambiguous observation of an angstrom-scale buckling structure in graphene is challenging, because the in-plane compression of the graphene lattice and the out-of-plane displacement of carbon atoms may cause the atomic details to be hidden behind the information limit of conventional electron microscopic instruments. Recent advances in aberration-corrected transmission electron microscopy (TEM) have improved its resolution limit to the sub-angstrom level.[22] We employed a monochromated, aberration-corrected TEM with a field-emission gun, Libra 200MC, operating at 80 kV, to conduct this study. The electron monochromator and the objective lens spherical aberration corrector modified the envelope function and the contrast transfer function relative to those of conventional field-emission TEM, resulting in a narrower depth of field at the focal plane of image formation and directly interpretable atomic images.[22] In a typical bright-field TEM image of a flat graphene area, the Fourier spectrum of the image demonstrated that the in-plane information limit of this microscope was well adjusted down to 0.58 Å in this study (Supporting Information, Figure S1).

RESULTS AND DISCUSSION

The graphene was prepared by liquid-phase exfoliation of graphite in organic solvent, *N*-methyl-pyrrolidone (NMP).[20] The graphene dispersion was deposited onto a holey carbon grid and vacuum dried before loading into the electron microscope specimen chamber (see Methods). Only the graphene sheets suspended in the empty holes of the carbon grid were subjected to TEM analysis. A previous study found that the graphene sheets prepared in NMP by this method are free of oxidation and defects, that about 70% of them have no more than three layers and that about 28% are monolayers.[20] Our results were consistent with these findings.

In one layer of a free-standing graphene bilayer, we observed a one-dimensional (1D) periodic buckling structure with a

*Address correspondence to
youdong_mao@dfci.harvard.edu,
joseph_sodroski@dfci.harvard.edu.

Received for review November 20, 2010
and accepted December 24, 2010.

10.1021/nn103153x

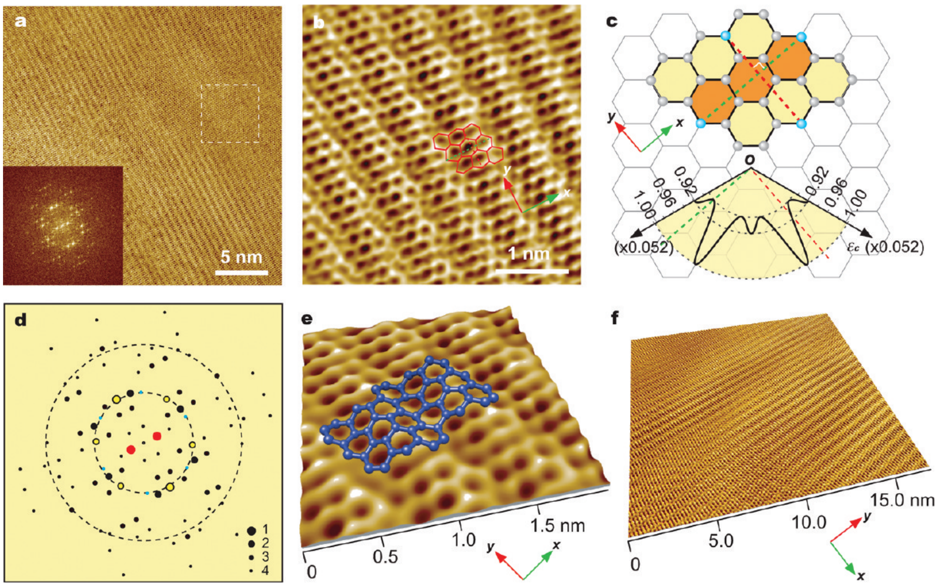

Figure 1. The 6.4 Å periodic buckling structure in a free-standing graphene bilayer. (a) TEM image of the buckling structure in one layer of a graphene bilayer. Inset, the Fourier spectrum of the image. The area bounded by the dashed box lacks buckling amplitude and coincides with a mesoscopic ripple. (b) Sub-angstrom resolution TEM reveals details of the reorganized carbon atoms and graphene lattices in the buckled region. The unit buckling manifold is marked by red hexagons. (c) The intrinsic geometric rule in the unit buckling manifold (upper panel) and the calculated angular distribution of nominal critical strain (ε_c) at a distance of three unit cells (lower panel, drawn in polar coordinate system) that guides the buckling orientation and wavelength selection. The green dashed line parallels the buckling direction. The red dashed line is orthogonal to the green dashed line. Only $2\pi/3$ angular range is shown for the angular distribution of ε_c due to its 6-fold symmetry. (d) The merged Fourier spectrum of the 6.4 Å buckling structure. The image quality (IQ) value,[29] from 1 to 4, is shown as the spot size from large to small. The red spots indicate the major buckling wavelength at 6.4 Å. The yellow spots indicate the major diffractions arising from the original graphene lattices. The blue spots indicate the reflections from the other nonbuckled layer of the graphene bilayer, which has about a $\pi/6$ rotation relative to the buckled layer. (e) The 3D reconstruction of the topographic view of the periodic buckling structure. The DFT-calculated 3D atomic configuration of the buckling structure with the lowest deformation energy (0.24 eV/atom) at the observed strain (0.09 in the *x*-direction), shown as a blue ball−stick model, was fitted into the 3D map. The buckling amplitude in the *x*-direction was determined to be ~1.2 Å; no obvious amplitude is observed in the *y*-direction. (f) The 3D perspective view of the buckling structure reconstructed from a TEM image demonstrates that the 6.4 Å buckling structure is nested within the mesoscopic ripples. In (b−f), the green arrows indicate the buckling orientation (*x*-direction), and the red arrows indicate the orthogonal *y*-direction.

wavelength of 6.4 ± 0.8 Å that is approximately composed of three consecutive unit cells of the hexagonal lattice, as shown in Figure 1. A sub-angstrom resolution TEM image (Figure 1b) shows that the periodic behavior of the buckling is strongly suppressed in the dimension orthogonal to the buckling orientation. The minimum unit of the buckling manifold may be approximately modeled by a 3 × 3 array of graphene's unit cells, whose three-dimensional (3D) structure lacks symmetry (Figure 1e). Only mesoscopic, randomly distributed ripples and no angstrom-scale buckling behaviors were observed in the other layer of the graphene bilayer.

Another buckling structure with a wavelength of 3.6 ± 0.5 Å was found in a folded graphene monolayer in the vicinity of the folding edge (Figure 2). The unit manifold in the major buckling direction comprises only two hexagonal unit cells (Figure 3a and b). This represents an extreme case for a buckled graphene layer, because a buckling wavelength comprising just one unit cell would generate at least 10 times higher deformation energy than that generated by the currently observed atomic conformation [24,25] and thus is energetically prohibited. Figure 3a clearly shows that the seemingly 1D buckling texture is actually decorated in detail by a highly ordered 2D array of unit buckling manifolds, each of which is composed of a 2 × 3 array of unit cells (Figure 3b). The 3D structure of the unit buckling manifold (Figure 3d) demonstrates twofold centrosymmetry (*P*2). Because the buckling in the *x*-direction markedly increases the bending rigidity in the *y*-direction,[24,25] a 2 × 3 array of unit cells might be the smallest unit configuration for spontaneous periodic buckling in graphene. The TEM images of the buckling structures (Figures 1−3) are not consistent with moiré fringe patterns of graphene bilayers (Supporting Information, note S1 and Figure S2).

Crystallographic analyses of the angstrom-scale buckling structures suggest common rules for the selection of buckling orientation and wavelength that are intrinsic to the geometry of the graphene lattice. In the 6.4 Å buckling structure, the buckling direction parallels the line intersecting the two most distant carbon atoms with *P*2 symmetry in three consecutive hexagonal cells, as illustrated in Figure 1c. A similar rule governs the 3.6 Å buckling structure, where the two

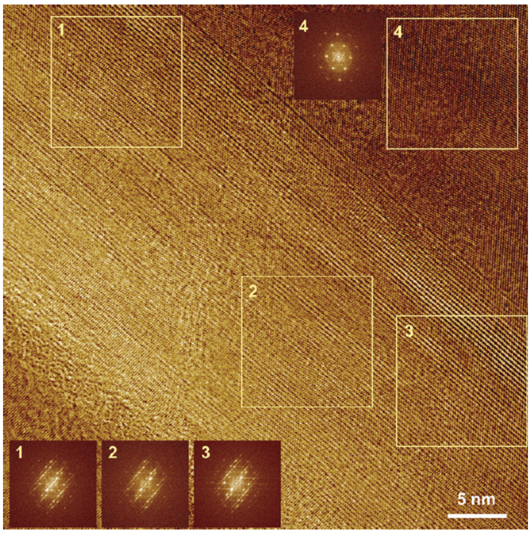

Figure 2. Aberration-corrected high-resolution TEM image of 3.6 Å periodic buckling in a folded graphene monolayer. Four image areas, boxed by yellow lines and numbered, are associated with the correspondingly numbered Fourier spectra in the insets. Comparison of Fourier spectra 1−3 suggests that they share a common major structure, though they have slight changes in minor features indicated by the diffraction spots beyond 1.0 Å. The major buckling direction orients strictly perpendicular to the folding line. Box 4 shows the background planar graphene sheet, providing an *in situ* control for crystallographic analysis.

most distant carbon atoms with *P*2 symmetry in two neighboring hexagonal cells define the major buckling orientation (Figure 3b). These geometry rules directly link the selection of buckling orientation to the wavelength. Furthermore, the folding direction in the 3.6 Å buckling structure is precisely orthogonal to the major buckling orientation (Figures 2 and 3b). The 3.6 Å buckling structure extends to the folding edge that defines the boundary condition of the overall buckling manifold; this observation suggests that the buckling and folding behaviors are highly coupled under the same geometry rules.

According to the classic theory of the Euler buckling instability, the critical strain (ε_c) of compression gives rise to the onset of buckling.[23,24] Below ε_c, there is only in-plane deformation for the graphene lattice. To understand the energetic basis of the observed geometry rules, we calculated ε_c at a distance of two or three unit cells as a function of the chiral direction (see Supporting Information, note S2 for details). The results, shown in lower panels in Figures 1c and 3b, reveal that the buckling orientations in the 6.4 and 3.6 Å buckling structures correspond to the smallest ε_c in its angular distribution at the distance of three and two unit cells, respectively. Thus, the buckling spontaneously chooses the direction of the lowest buckling energy matching its wavelength. To ascertain this result, we performed first-principles calculations of the buckling structures using the density functional theory (DFT) (see Methods). The *ab initio* graphene structures of the lowest deformation energy under compression buckle exactly along the experimentally observed directions; the entire atomic configurations closely match the 3D buckling structures reconstructed from the *Z* contrast of the TEM micrographs (Figures 1e and 3d). The consistency between experimental observations, *ab initio* calculations and Euler buckling theory, implies that the geometry rules are intrinsic properties of graphene's buckling at this fine level and are independent of specific interactions between graphene and other materials (like solvents or TEM grids). This contrasts with the mesoscopic periodic ripples,[16−19] where no similar intrinsic geometry rules were observed. Rather, their behaviors are highly dependent on the specific interaction between graphene and substrate and are governed by the mesoscopic elasticity of graphene sheets,[16,24−27] where the geometric details of the graphene lattice work in a mean-field manner.

More intriguingly, the overall buckling manifolds demonstrate geometric complexity with cascaded features. The 6.4 Å buckling structure was seen to be nested within randomly distributed ripples with sizes between 5 to 20 nm (Figure 1a and f) that are strongly reminiscent of the irregular ripples observed in suspended and supported graphene.[6−8] Similarly, the 3.6 Å buckling structure was nested within another 1D periodic ripple with a wavelength of 2−3 nm and with the same buckling direction (Figures 2 and 3e). However, the 1D nanoscale periodic ripple structure has relatively weak periodicity (with the wavelength varying slightly at different places), resembling the trench-induced mesoscopic ripples in graphene.[16] Strong evidence for the nesting of the 3.6 Å buckling structure into nanoscale periodic ripples is that the original diffraction peaks of the graphene lattice in the Fourier spectrum are broadened into lines strictly along the buckling direction (Figures 2 and 3c); this indicates that the angstrom-scale structures are embedded within a one-dimensionally curved 3D manifold. Although cascaded buckling has been observed in deformed plastic sheets,[28] it is unexpected in 2D crystalline sheets like graphene. Taken together, our findings suggest that the angstrom-scale buckling and the mesoscopic rippling are manifestations of distinct mechanical properties of graphene that may coexist in a linearly combined fashion.

To understand the potential changes in the physical properties of graphene arising from the angstrom-scale periodic buckling, we used DFT to calculate the electronic structures of the buckled graphene monolayers (see Supporting Information and Methods). The low-energy charge carriers in pristine graphene are well described by a massless Dirac equation and have a linear energy dispersion isotropic near the Dirac points (*K*) at the corners of the Brillouin zone (Figure 4a).[2] A previous theoretical study clarified that an anisotropy in energy dispersion near the Dirac points is realizable

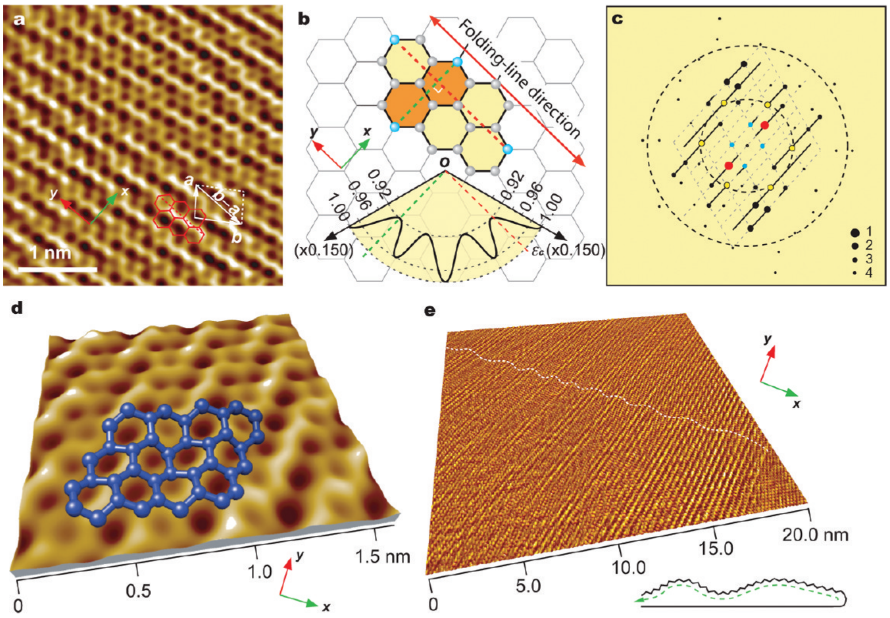

Figure 3. The 3.6 Å periodic buckling structure in a folded graphene monolayer. (a) Sub-angstrom resolution TEM imaging of the buckling structure in detail. The unit manifold is marked by red hexagons. Arrows a and b dictate the lattice vectors of the periodic buckling structure, where b−a is parallel to the *y*-direction. (b) The intrinsic geometric rule in the unit buckling manifold (upper panel) and the calculated angular distribution of the nominal critical strain (ε_c) at a distance of two unit cells (lower panel, drawn in polar coordinate system) that guides the buckling orientation and wavelength selection. The green dashed line parallels the buckling direction (*x*-direction). The red dashed line parallels the folding line (*y*-direction). Only $2\pi/3$ angular range is shown for the angular distribution of ε_c due to its 6-fold symmetry. (c) The merged Fourier spectrum of the 3.6 Å buckling structure. The IQ, from 1 to 4, is shown as the spot size. The red spots indicate the major buckling periodicity at 3.6 Å. The blue spots indicate the 2D lattice of the unit buckling manifold, corresponding to the lattice vectors a and b shown in panel (a). The yellow spots indicate the major diffractions arising from the original graphene lattice. (d) The 3D reconstruction of the topographic view of the buckling structure. The DFT-calculated 3D atomic configuration of the buckling structure with the lowest deformation energy (0.77 eV/atom) at the observed strain (0.15 in the *x*-direction and 0.04 in the *y*-direction), shown as a blue ball−stick model, was fitted into the 3D map. The buckling amplitude is greater in the *x*-direction (∼0.9 Å) than in the *y*-direction (∼0.3 Å). (e) The 3D perspective view of the buckling structure shows that the 3.6 Å buckling structure is nested within another set of 1D ripples of 2−3 nm wavelength with the same propagation direction. The white dashed line highlights the nanoscale ripples. There is more contrast and a slightly larger wavelength of the 3.6 Å buckling structure at the ripple top, as schematically modeled in the inset. In all panels, the green arrows indicate the major buckling orientation, and the red arrows indicate the folding-line direction.

in graphene under externally applied periodic potentials, owing to the chiral nature of charge carriers.[5] Our *ab initio* results suggest that the chirality may also give rise to a significant anisotropy in the energy dispersion of charge carriers in the angstrom-scale buckled graphene monolayers in the absence of external periodic potentials (Figure 4b−f). The Dirac cone in pristine graphene is circular and centered at the Dirac point (Figure 4a and d). By contrast, in the buckled graphene, the Dirac cone is significantly broadened and becomes oval; its horizontal cross-section is no longer centered at the Dirac point (Figure 4b−f). Such strong symmetry breakage implies a highly anisotropic propagation of charge carriers through graphene with the angstrom-scale buckling structures.[5] Other changes in graphene's properties induced by the angstrom-scale buckling are thus expected and deserving of systematic study.

The formation of the angstrom-scale buckling structures is expected to arise from the interlayer interactions in a bilayer or a folded monolayer with the assistance of liquid-phase processing (see Supporting Information, notes S3−S5 for details). The potential utilization of these fine buckling structures might ultimately allow miniaturization of strain-engineered graphene devices to several angstroms.[13−15] The anisotropic behaviors of massless Dirac fermions in the angstrom-scale buckling structures may endow graphene electronic circuits and devices with novel functions and utilities.[5] The substrate-free production of the periodic buckling structures also allows great flexibility in adapting them for diverse potential applications.

METHODS

Sample Preparation. Graphite flakes with a size of 1.8−5 mm (NGS Naturgraphit GmbH, Leinburg, Germany) were incubated in 1 mL *N*-methyl-pyrrolidinone (NMP, HPLC level, > 99%, Sigma-Adlrich) in a 1.5 ml glass vial and sonicated for 3 h in an ultrasonication bath (Input 160 W, output 70 W; Branson 1510, CT). The sonicated solution was then centrifuged at 500 rpm for 90 min. The upper suspension was decanted off the vial

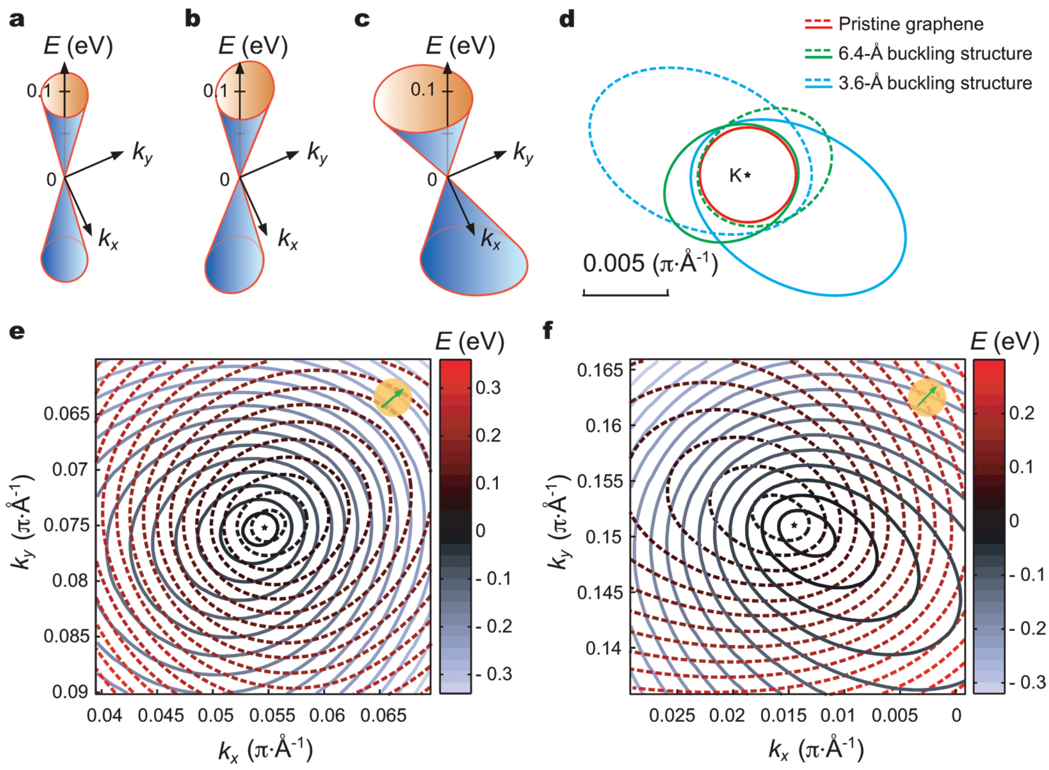

Figure 4. Anisotropic changes in the electronic structure of graphene induced by angstrom-scale buckling. (a) The isotropic energy dispersion near one of the Dirac points of charge carriers in pristine graphene. (b and c) The anisotropic energy dispersion near the Dirac points of charge carriers in graphene with the 6.4 and 3.6 Å buckling structures, respectively. The 3D plots in (a−c) are shown on the same scale. (d) Comparison of the energy dispersion at the same contour level ($E = 0.05$ eV as dashed lines, and $E = -0.05$ eV as solid lines) of pristine and buckled graphene, showing significant anisotropic changes induced by the angstrom-scale buckling. The Dirac points for the different structures are shifted and aligned to the same position in the *k* plane for comparison, as indicated by a black asterisk. (e and f) The contour plots of the energy dispersion around the Dirac points of charge carriers in graphene with the 6.4 and 3.6 Å buckling structures, respectively. The contours above the Dirac points are shown as dashed lines and the contours below the Dirac points by solid lines. The position of Dirac point at the center of each contour plot is marked by asterisk. The green arrows in (e and f) indicate the major buckling directions and correspond to the green arrows shown in Figures 1 and 3, respectively.

and was transferred to another clean vial for storage before use. The precipitated graphite flakes may be used again by exfoliation in another volume of the solvent. A 3 μL droplet of the graphene dispersion was applied to a holey carbon grid (C-Flat, 400 mesh size, 1.2/1.3R, Protochips, NC) and blotted by filter paper from the edge and backside of the grid. (A second droplet of the graphene dispersion may be applied to the same grid, which enhances the chance of observing the buckling structures.) The grid was then vacuum dried for 30−60 min before loading into the electron microscope specimen chamber.

TEM Analysis. The monochromated, aberration-corrected TEM (Libra 200MC, Carl Zeiss NTS, MA) equipped with a field-emission gun (80−200 kV) and an in-column omega energy filter was first aligned and adjusted with respect to the objective lens aberration corrector at 80 kV, with the monochromator and energy filter off, using an amorphous carbon film area, through the CETCOR software interface (CEOS GmbH, Heidelberg, Germany). After the objective lens spherical aberration was corrected up to the third order, the monochromator was switched in (4 μm slit). TEM imaging and analysis then were performed at near-Gaussian focus at room temperature and recorded by a 4000 × 4000 CCD camera (Gatan, Ultrascan4000, USA) at a nominal magnification of 1 000 000×. All image data reported in this paper were based on the same aberration correction parameters. Because of the integration of *Z*-axis density, transmission electron mirographs do not directly measure the sample height. Nonetheless, the height of rippling in 2D materials can still be estimated by either the *Z* contrast change of the atom volume or the geometric constraint of the atomic crystal order. In this work, we employed the latter approach, taking advantage of the rich information in atomic positions in the $x-y$ plane and verified the results by DFT. Using the crystallographically analyzed geometric configuration of the unit buckling structure as shown in Figures 1c and 3b and assuming the average carbon−carbon bond length to be 1.42 Å, one can readily estimate the rippling height. The estimation gave 0.9 ± 0.3 Å for the 6.4 Å buckling structure, in agreement with the DFT result 1.2 Å, and 1.1 ± 0.3 and 0.5 ± 0.3 Å in the *x*- and *y*-directions, respectively, for the 3.6 Å buckling structure, agreeing with the DFT results of 0.9 (*x*) and 0.3 Å (*y*).

Theoretical Analysis and First-Principles Calculations. To calculate the critical strain ε_c as a function of chiral direction, we used a quantitative relationship (eq 1 in Supporting Information) that was yielded by a molecular mechanics simulation of graphene elasticity without imposing the approximation of continuum mechanics.[24] The calculation details are provided in Supporting Information, note S2 and Figure S3. The first-principles calculations were performed with the software package Spanish Initiative for Electronic Simulations with Thousands of Atoms (SIESTA) that implements the DFT.[30] The atomic structures, deformation energy, and band structures were calculated using localized atomic orbitals with an energy cutoff of 70 Ry (~952 eV). To calculate the atomic structures of the angstrom-scale buckling, the supercells containing 9 and 6 graphene unit cells (Figures 1c and 3b) were used for the 6.4 and 3.6 Å buckling structures, respectively. The structures were relaxed under given strains and periodic boundary conditions. The energy optimization was terminated when the magnitude of the force on each atom was less than 0.04 eV Å^{-1}. For the calculation of the 3.6 Å buckling structure, an extra geometric constraint exerted by the folding edge was taken into account; that is, in the supercell, 7 carbon atoms located around a line parallel to the folding edge were limited in the extent of their out-of-plane displacement to ≤0.3 Å. No extra geometric constraint was used for the calculation of the 6.4 Å buckling structure. In all calculations, the Perdew−Burke−Ernzerhof exchange−correlation functional and a *k*-point mesh cutoff of 20 Å were used. As the *ab initio* atomic models of the buckling structures closely match the 3D reconstructions of the buckling structures generated by the *Z* contrast images of aberration-corrected TEM, the 3D coordinates of the *ab initio* atomic structures were used to extract the amplitudes of the buckling structures and were used as input parameters for the *ab initio* calculations of their corresponding energy dispersion. Although the *ab initio* calculations produced detailed atomic configurations that can directly explain the TEM observations, they alone cannot account for the selection of the angstrom-scale buckling wavelength. Instead, a semi-quantitative analysis is described in Supporting Information, note S4, that accounts for the selection of angstrom-scale wavelength, by combining results from the *ab initio* calculations and the dynamic theory of Euler buckling instability.

Acknowledgment. The authors thank D. C. Bell for assis tance and coordination in TEM imaging and maintenance and M. Lemme and Q. Ouyang for insightful discussion and comments. This work was supported by the National Institute of Health (NIH) (AI67854) and the Ragon Institute of MGH, MIT, and Harvard. The experiment was performed in part at the Center for Nanoscale Systems (CNS), a member of National Nanotechnology Infrastructure Network (NNIN), which is supported by the National Science Foundation under NSF award no. ECS-0335765. C.N.S. is part of the Faculty of Arts and Sciences at Harvard University.

Supporting Information Available: Details on TEM analysis and theoretical analysis, exclusion of the possibility that the TEM images of the buckling structures result from moiré fringe patterns, calculation of the critical strain as a function of chiral direction, a possible mechanism for the formation of the angstrom-scale periodic buckling, the selection of an angstrom-scale buckling wavelength, and symmetry breaking and reduced dimensionality of buckling. This material is available free of charge *via* the Internet at http://pubs.acs.org.

REFERENCES AND NOTES

1. Novoselov, K. S.; Geim, A. K.; Morozov, S. V.; Jiang, D.; Zhang, Y.; Dubonos, S. V.; Grigorieva, I. V.; Firsov, A. A. Electric Field Effect in Atomically Thin Carbon Films. *Science* **2004,** *306*, 666–669.
2. Novoselov, K. S.; Geim, A. K.; Morozov, S. V.; Jiang, D.; Katsnelson, M. I.; Grigorieva, I. V.; Dubonos, S. V.; Firsov, A. A. Two-Dimensional Gas of Massless Dirac Fermions in Graphene. *Nature* **2005,** *438*, 197–200.
3. Oostinga, J. B.; Heersche, H. B.; Liu, X.; Morpurgo, A. F; Vandersypen, L. M. K. Gate-Induced Insulating State in Bilayer Graphene Devices. *Nat. Mater.* **2008,** *7*, 151–157.
4. Zhang, Y.; Tang, T. T.; Girit, C.; Hao, Z.; Martin, M. C.; Zettl, A.; Crommie, M. F.; Shen, Y. R.; Wang, F. Direct Observation of a Widely Tunable Bandgap in Bilayer Graphene. *Nature* **2009,** *459*, 820–823.
5. Park, C. H.; Yang, L.; Son, Y. W.; Cohen, M. L.; Louie, S. G. Anisotropic Behaviours of Massless Dirac Fermions in Graphene under Periodic Potentials. *Nat. Phys.* **2008,** *4*, 213–217.
6. Meyer, J. C.; Geim, A. K.; Katsnelson, M. I.; Novoselov, K. S.; Booth, T. J.; Roth., S. The Structure of Suspended Graphene Sheets. *Nature* **2007,** *446*, 60–63.
7. Fasoline, A.; Los, J. H.; Katsnelson, M. I. Intrinsic Ripples in Graphene. *Nat. Mater.* **2007,** *6*, 858–861.
8. Geringer, V.; Liebmann, M.; Echtermeyer, T; Runte, S.; Schmidt, M.; Ruckamap, R.; Lemme, M. C.; Morgenstern, M. Intrinsic and Extrinsic Corrugation of Monolayer Graphene Deposited on SiO_2. *Phys. Rev. Lett.* **2009,** *102*, 076102.
9. Morozov, S. V.; Novoselov, K. S.; Katsnelson, M. I.; Schedin, F.; Ponomarenko, L. A.; Jiang, D.; Geim, A. K. Strong Suppression of Weak Localization in Graphene. *Phys. Rev. Lett.* **2006,** *97*, 016801.
10. Herbut, I. F.; Juricic, V.; Vafek, O. Coulomb Interaction, Ripples, and the Minimal Conductivity of Graphene. *Phys. Rev. Lett.* **2008,** *100*, 046403.
11. Elias, D. C.; Nair, R. R.; Mohiuddin, T. M. G.; Morozov, S. V.; Blake, P.; Halsall, M. P.; Ferrari, A. C.; Boukhvalov, D. W.; Katsnelson, M. I.; Geim, A. K.; et al. Control of Graphene's Properties by Reversible Hydrogenation: Evidence for Graphene. *Science* **2009,** *323*, 610–613.
12. Boukhvalov, D. W.; Katsnelson, M. I. Tuning the Gap in Bilayer Graphene using Chemical Functionalization: Density Functional Calculations. *Phys. Rev. B* **2008,** *78*, 085413.
13. Pereira, V. M.; Castro Neto, A. H. Strain Engineering of Graphene's Electronic Structure. *Phys. Rev. Lett.* **2009,** *103*, 046801.
14. Guinea, F.; Horovitz, B.; Le Doussal, P. Gauge Field Induced by Ripples in Graphene. *Phys. Rev. B: Condens. Matter Mater. Phys.* **2008,** *77*, 205421.
15. Guinea, F.; Katsnelson, M. I.; Geim, A. K. Energy Gaps and a Zero-Field Quantum Hall Effect in Graphene by Strain Engineering. *Nat. Phys.* **2010,** *6*, 30–33.
16. Bao, W.; Miao, F.; Chen, Z.; Zhang, H.; Jang, W.; Dames, C.; Lau, C. N. Controlled Ripple Texturing of Suspended Graphene and Ultrathin Graphite Membranes. *Nat. Nanotechnol.* **2009,** *4*, 562–566.
17. Vazquez de Parga, A. L.; Calleja, F.; Borca, B.; Passeggi, M. C. G., Jr.; Hinarejos, J. J.; Guinea, F.; Miranda, R. Periodically Rippled Graphene: Growth and Spatially Resolved Electronic Structure. *Phys. Rev. Lett.* **2008,** *100*, 056807.
18. N'Diaye, A. T.; Bleikamp, S.; Feibelman, P. J.; Michely, T. Two-Dimensional Ir Cluster Lattice on a Graphene Moiré on Ir(111). *Phys. Rev. Lett.* **2006,** *97*, 215501.
19. Sutter, P.; Sadowski, J. T.; Sutter, E. Graphene on Pt(111): Growth and Substrate Interaction. *Phys. Rev. B: Condens. Matter Mater. Phys.* **2009,** *80*, 245411.
20. Hernandez, Y.; Nicolosi, V.; Lotya, M.; Blighe, F. M.; Sun, Z.; De, S.; Mcgovern, I. T.; Holland, B.; Byrne, M.; Gun'ko, Y. K.; et al. High-Yield Production of Graphene by Liquid-Phase Exfoliation of Graphite. *Nat. Nanotechnol.* **2008,** *3*, 563–568.
21. Li, X.; Zhang, G.; Bai, X.; Sun, X.; Wang, X.; Wang, E.; Dai, H. Highly Conducting Graphene Sheets and Langmuir-Blodgett Films. *Nat. Nanotechnol.* **2008,** *3*, 538–542.
22. Batson, P. E.; Dellby, N.; Krivanek, O. L. Sub-Ångstrom Resolution Using Aberration Corrected electron optics. *Nature* **2002,** *418*, 617–620.
23. Golubovic, L.; Moldovan, D.; Peredera, A. Dynamics of the Euler Buckling Instability. *Phys. Rev. Lett.* **1998,** *81*, 3387–3390.
24. Lu, Q.; Huang, R. Nonlinear Mechanics of Single-Atomic-Layer Graphene Sheets. *Int. J. Appl. Mech.* **2009,** *1*, 443–467.
25. Lu, Q.; Arroyo, M.; Huang, R. Elastic Bending Modulus of Monolayer Graphene. *J. Phys. D: Appl. Phys.* **2009,** *42*, 102002.
26. Cadelano, E.; Palla, P. L.; Giordano, S.; Colombo, L. Nonlinear Elasticity of Monolayer Graphene. *Phys. Rev. Lett.* **2009,** *102*, 235502.
27. Lee, C.; Wei, X.; Kysar, J. W.; Hone, J. Measurement of the Elastic Properties and Intrinsic Strength of Monolayer Graphene. *Science* **2008,** *321*, 385–388.
28. Sharon, E.; Roman, B.; Marder, M.; Shin, G. S.; Swinney, H. L. Buckling Cascades in Free Sheets. *Nature* **2002,** *419*, 579.
29. Glaeser, R. M.; Downing, K.; DeRosier, D.; Chiu, W.; Frank, J. *Electron Crystallography of Biological Macromolecules*; Oxford University Press: New York, 2007.
30. Soler, J. M.; Artacho, E.; Gale, J. D.; Garcia, A.; Junquera, J.; Ordejon, P.; Sanchez-Portal, D. The SIESTA Method for *ab initio* Order-N Materials Simulation. *J. Phys.: Condens. Matter* **2002,** *14*, 2745–2779.

Supporting Information for the paper:

Graphene structures at an extreme degree of buckling

Youdong Mao[1], Wei L. Wang[2], Dongguang Wei[3], Efthimios Kaxiras[2], & Joseph G. Sodroski[1,4]

[1]Dana-Farber Cancer Institute, Department of Pathology, Harvard Medical School, Boston, Massachusetts 02115, USA. [2]Department of Physics, School of Engineering and Applied Sciences, Harvard University, Cambridge, Massachusetts 02138, USA. [3]Carl Zeiss SMT, Inc., One Corporation Way, Peabody, Massachusetts 01960, USA. [4]Department of Immunology and Infectious Disease, Harvard School of Public Health, Boston, Massachusetts 02115, USA

Supporting Notes

S1. Exclusion of the possibility that the TEM images of the buckling structures result from moiré fringe patterns

We considered the possibility that the observed TEM images of the observed periodic patterns did not result from true buckling structures, but are artefacts due to moiré fringe effects. Moiré fringe is an interference pattern created from rotation (or displacement) between two overlaid lattice structures. Several pieces of evidence help to exclude moiré fringe effects as an explanation of the observed ångstrom-scale patterns. First, we simulated the possible moiré fringe patterns from two graphene layers that are overlaid at orientations consistent with those deduced from our observations of the 6.4-Å and 3.6-Å buckling structures. As shown in Supporting Fig. S2a, c-f, all of these simulations have six-fold centrosymmetry, which are not observed in our TEM images of the structures. Moreover, we also simulated the moiré fringe patterns from a uniaxially and biaxially strained graphene layer overlaid on an unstrained graphene layer, with typical results (shown in Supporting Fig. S2g-l) that produce the periodicities comparable to the experimental observations. See Fig. S2 legend for more details. However, all these moiré fringe patterns are clearly very different from the TEM images of the 6.4-Å and 3.6-Å buckling structures. For monochromated aberration-corrected TEM imaging, when the illumination is precisely focused on one of the graphene layers, the information from other layers will be largely phased out. This is why the deflection peaks in the Fourier spectrum of the second, flat, out-of-focus graphene monolayer are 10-times weaker than those of the on-focus buckled graphene monolayer. This also explains why we were able to avoid observing the 6-fold symmetric moiré fringe pattern. Second, the transverse direction of the moiré fringe should be located precisely in the middle of the two (n,0)-directions of the two overlaid lattice structures. For the TEM images of the 6.4-Å buckling structure, the transverse direction is far away from the middle direction of the two layers that are overlaid with a rotation of 30°. For the images of the 3.6-Å buckling structure, although the major buckling direction (the x-direction in Fig. 3 of the paper) is consistent with this rule, the second buckling direction of weaker amplitude (the y-direction in Fig. 3 of the paper) is not. Third, any rippling curvature in one of the two layers will give rise to an in-plane curvature of the moiré fringe, instead of the cancelling of the fringe (weakening of the amplitude) in a local area. In our TEM images of the 6.4-Å buckling structure, some local areas with weakened amplitude are not consistent with these expectations for a moiré fringe effect. However, the observation can be well explained by mesoscopic ripples structurally weakening the amplitude of the 6.4-Å buckling structure because it gives rise to a larger out-of-plane displacement of carbon atoms. A similar point of view applies to the TEM observation of the 3.6-Å buckling structure. Fourth, an image resulting from moiré fringe will not give rise to directly interpretable atomic models of the buckling structures of a graphene monolayer and instead should introduce ambiguity into the fitting of atomic models of the monolayer. This is well demonstrated in the Supplementary Figs S2a and b, where we do capture a TEM image of the moiré fringe by setting the focus between two layers. The observed pattern is highly consistent with the computer-simulated fringe pattern and cannot be explained by any distorted structure of a single-layer graphene. Conversely, our sub-ångstrom TEM images for the buckling structures can be readily fitted with the DFT-calculated atomic models of the buckling structures with the lowest deformation energy under the observed strains, and there is no ambiguity encountered. Fifth, the transition area between areas with and without the ångstrom-scale buckling, shown in Supporting Fig. S5, provides evidence that the TEM images of the 6.4-Å buckling structure do not result from the moiré fringe pattern; moiré fringe patterns are not expected to exhibit a smooth transition into disappearance such as that shown in this image. In summary, our imaging method is well controlled to avoid the observation of moiré fringe patterns. Multiple lines of evidence suggest that the sub-ångstrom TEM images of the buckling structures reported in this paper do not result from moiré fringe patterns.

S2. Calculation of the critical strain as a function of chiral direction

The well-known Euler buckling instability describes the phenomena that a compressed rod (or plate) buckles out sideways if the compressive strain ε exceeds the critical value $\varepsilon_c \sim L^{-2}$, where L is the length of the rod (or plate). Below the critical strain ε_c, there is only in-axis deformation for the rod (or in-plane deformation for the plate). Historically, Euler buckling instability is the very first example of bifurcation phenomena and a paradigm for subsequent theories of phase transition. Buckling involves a spontaneous symmetry break. A compressed membrane may buckle either up or down, whereas a compressed rod may be buckled out sideways in an arbitrary direction. A recent study of molecular mechanics (MM) simulations[24], based on the crystal structure of a graphene monolayer without imposing any approximation of continuum mechanics, yielded an analytical form of the critical nominal strain for the onset of buckling in a graphene ribbon

$$\varepsilon_c = \frac{4\pi^2 D}{C_{11} L^2} \tag{1}$$

where D is the bending modulus of the graphene membrane, L is the ribbon width along the load direction, and C_{11} is the in-plane elastic modulus of graphene at infinitesimal strain. Equation (1) is totally consistent with the Euler buckling theory, substantiating that this theory is valid for a graphene lattice on the atomic level.

In this work, we consider the calculation of the critical strain as a function of chiral direction, for a given wavelength of three and two unit cells in all chiral directions. When we consider a fixed wavelength of three unit cells for all chiral directions, and translate it to an effective L that is related to ε_c via equation (1), it is equivalent to measuring the effective width of the graphene ribbon shown in Supporting Fig. S3a. In this case, one should consider the smallest unit in which a local compressive strain is established between the nearest inter-layer contact-points, on which compressive force is exerted, instead of considering the entire structure. On the other hand, one should note that buckling at such a small length scale is not continuous in space, because structural change can only happen at the bond angle, bond dihedral angle, and bond length (Buckling cannot happen inside a single chemical bond). This is the major difference between ångstrom-scale buckling and mesoscopic buckling. In the latter case, the graphene layer can be modelled as a continuum, whereas this is not true in the former case. With this in mind, it is straightforward to deduce the mathematical form of the effective $L(\theta)$, where θ is defined as the angle of the chiral direction relative to the zigzag direction (dashed straight line in Supporting Fig. S3). Because of the six-fold symmetry of $L(\theta)$, a calculation in the range of $0\text{–}2\pi/3$ radians would suffice for comparison with experimental observations. For the size of three unit cells, we have

$$L(\theta)=\begin{cases} 3\sqrt{3}r_0\sec\theta & 0\le\theta<\alpha \\ 5r_0\sec(\frac{\pi}{6}-\theta) & \alpha\le\theta<\frac{\pi}{3}-\alpha \\ 3\sqrt{3}r_0\sec(\frac{\pi}{3}-\theta) & \frac{\pi}{3}-\alpha\le\theta<\frac{\pi}{3}+\alpha \\ 5r_0\sec(\frac{\pi}{2}-\theta) & \frac{\pi}{3}+\alpha\le\theta<\frac{2\pi}{3}-\alpha \\ 3\sqrt{3}r_0\sec(\frac{2\pi}{3}-\theta) & \frac{2\pi}{3}-\alpha\le\theta<\frac{2\pi}{3} \end{cases} \tag{2}$$

where r_0 is the carbon-carbon sp^2 bond length, usually taken as 1.42 Å, and $\alpha = \cot^{-1}(3\sqrt{3})$. For the size of two unit cells, we have

$$L(\theta)=\begin{cases} 2\sqrt{3}r_0\sec\theta & 0\le\theta<\beta \\ \frac{7r_0}{2}\sec(\frac{\pi}{6}-\theta) & \beta\le\theta<\frac{\pi}{3}-\beta \\ 2\sqrt{3}r_0\sec(\frac{\pi}{3}-\theta) & \frac{\pi}{3}-\beta\le\theta<\frac{\pi}{3}+\beta \\ \frac{7r_0}{2}\sec(\frac{\pi}{2}-\theta) & \frac{\pi}{3}+\beta\le\theta<\frac{2\pi}{3}-\beta \\ 2\sqrt{3}r_0\sec(\frac{2\pi}{3}-\theta) & \frac{2\pi}{3}-\beta\le\theta<\frac{2\pi}{3} \end{cases} \tag{3}$$

where $\beta = \cot^{-1}(2\sqrt{3})$. By substitution of equations (2), (3) into equation (1), the angular distributions of $\varepsilon_c(\theta)$ can be readily calculated, as shown in Fig. 1c and Fig. 3b in the paper, respectively. In the calculation, we assume that the bending modulus D and the in-plane elastic modulus C_{11} are isotropic, namely, independent of the chiral direction. In fact, this is true as shown in several simulation and theoretical studies[23-25], because the D and C_{11} values that determine the ε_c correspond to the ground state of the graphene ribbon, where nonlinear effects of the bending modulus and in-plane elastic modulus have not yet begun to play a role. Moreover, D/C_{11} is taken as the value that yields $\varepsilon_c = 0.0068$ at $L = 1.97$ nm, which is determined from the MM simulation in Ref. 24 of the paper. In Ref. 24, the authors also showed that ε_c is insensitive to the chiral direction for a mesoscopic (nanoscale or micron-scale) graphene ribbon. As we calculated herein, ε_c does become more sensitive to the chiral direction at the ångstrom scale, and its anisotropy becomes high enough to affect the spontaneous selection of buckling orientation.

S3. A possible mechanism for the ångstrom-scale periodic buckling

Combining the experimental procedure of liquid-phase processing of graphene with our sub-ångstrom resolution TEM imaging and electron crystallography, we propose a possible mechanistic model for the formation of the ångstrom-scale periodic buckling structures, schematically illustrated in Supporting Fig. S4. A free-standing graphene monolayer produced by the liquid-phase exfoliation of graphite can hardly stay in a perfect 2D plane over a long distance in solvent[6,7]. Because of the intrinsic curvature in graphene driven by thermal fluctuations[6], some bulge areas with solvent sandwiched inside may form between two partially adhered monolayers (Supporting Fig. S4a), or between the two sides of a folded and partially self-adhered monolayer (Supporting Fig. S4b). Importantly, the stepwise removal of the solvent could transform the curvature in the bulge area into in-plane compressive strain, which promotes stepwise buckling with ångstrom-scale wavelengths, possibly aided by in-plane recessive movement of the meniscus interface of the sandwiched solvent (see Supporting Fig. S4 legend for a detailed description). This mechanism suggests that the ångstrom-scale buckling structure in graphene may be introduced by appropriately manipulating the inter-layer interaction in a bilayer or a folded monolayer in liquid phase without the assistance of specific substrates.

There are several observations supporting the proposed mechanism for the formation of the ångstrom-scale buckling structures. First, we observed another graphene monolayer without ångstrom-scale buckling adhering to the graphene monolayer with the 6.4-Å buckling structure. The blue deflection peaks in Fig. 1d verified the existence of the associated monolayer has undergone a $\pi/6$ rotation with respect to the buckled monolayer. This observation is consistent with a model in which that the 6.4-Å buckling structure is formed with the aid of another graphene monolayer by solution-based processing. Second, for the 3.6-Å buckling structure formed in a folded graphene monolayer, we only observed buckling on one side of the folding line; there was no ångstrom-scale buckling observed on the other side of the folding line (Figs 2 and 3c of the paper), even though mesoscopic scale rippling could be detected. Third, for both the 6.4-Å and 3.6-Å buckling structures, we observed a transition from an area with ångstrom-scale buckling to an area without ångstrom-scale buckling in the same monolayer (Supporting Fig. S5 and Fig. 2 of the paper, respectively). For the 3.6-Å buckling structure, the transition region is exactly on the opposite side of the folding edge (Fig. 2 of the paper). These transition regions provide evidence that adherence of the two layers is important to buckling formation. Fourth, we were not able to find any ångstrom-scale buckling structures on free-standing single layers without attachment to another monolayer; however, mesoscopic rippling was generally observed on free-standing single layers, which was consistent with previous reports of mesoscopic ripples[6,7]. Finally, the analysis based on the classic and dynamic theories of the Euler buckling instability, described in the previous section (Note S2), provides another aspect of the consistency between the proposed mechanism and the intrinsic behaviours of the observed buckling structures. In other words, the proposed mechanism is supported by the dynamic theory of the Euler buckling instability. To summarize, the basic idea of the proposed mechanism is that the fine buckling structures in a graphene monolayer can only form upon interaction with another monolayer, which helps establish compressive strain in graphene, in the absence of any substrate. There is no reason for an isolated graphene monolayer to buckle at the ångstrom scale without extrinsic interactions leading to a compressive strain; previous studies have already established that thermal fluctuations give rise to mesoscopic ripples rather than ångstrom-scale buckling[6,7].

S4. The selection of an ångstrom-scale buckling wavelength

The good agreement of experimental observation and theoretical calculation substantiates the assertion that the buckling of graphene at the ångstrom scale spontaneously chooses the direction of lowest buckling energy. Such a point of view also gives a qualitative insight into the question of *how the buckling chooses an ångstrom-scale wavelength*. Here we evaluate the energetic feasibility and dynamic origin of the ångstrom-scale wavelength.

First, we consider a static picture of the energetic plausibility and stability of the ångstrom-scale buckling structures. There are two major factors that potentially contribute to relaxation of the ångstrom-scale buckling structures: thermal fluctuations and deformation energy. The in-plane relaxation force generated by the thermal fluctuations is estimated to below 0.1 eV / atom (refs 7, 31). To evaluate the impact of the deformation energy, we calculated the energy penalty incurred by each of the buckling structures by DFT. Our DFT results show that the deformation energies for the 6.4-Å and 3.6-Å structures are 0.24 and 0.77 eV / atom, respectively. These may be balanced by the inter-layer interactions between the two graphene layers. The inter-layer interactions are complicated when the lattice mismatch between two layers changes from place to place. For two perfectly flat graphene layers with Bernal phase[31] (*AB* stacking), the inter-layer interactions are dominated by weak van der Waals force (0.01 eV / atom at ~0.335 nm in the separation between layers[31-34]). However, a recent theoretical study[31] using DFT calculations suggests that two graphene layers stacked directly on top of each other (*AA* stacking) form stronger interactions (0.52 eV / atom lower than the Bernal phase, with an energy barrier from *AA* to *AB* stacking equalling 0.85 eV / atom, when the graphene lattice constant a = 0.291 nm, and the distance between planes d = 0.156 nm). Note that the energy barrier is large enough to overwhelm but remains on the same scale as the summation of the buckling energy and the thermal fluctuation energy. The theoretical analysis of *AA* stacking[31] is supported by previous experimental observations of *AA* stacking in multilayer graphene[35] and other similar carbon structures known as *n*-prismanes[36]. The authors of ref. 31 argued that this new polymorphic form for two stacked graphene layers is feasible at room temperature due to the sufficiently large activation energy necessary to destroy this phase, but may require some strain engineering to introduce the phase. In the graphene bilayer system described in this paper, it is obviously feasible that the strong lattice mismatch between the bilayer arising from the ångstrom-scale buckling in one layer could introduce *AA* stacking in local contacting areas, thus offering strong local interactions to prevent the local relaxation of the buckling structures. The second notable factor that counteracts the relaxation of buckling is that the collective effect of van der Waals interactions (0.5 eV nm^{-1}) outside the buckling areas can offer sufficient static friction to prevent the overall buckling structure from sliding in-plane against another layer. Moreover, another recent study suggests that the in-plane friction on the surfaces of 2D atomic crystals increases with decreases in the number of layers in the stacked 2D crystals[37]. The friction between one or two layers increases up to about 200% of those frictional forces in the multilayer (> 4 layers) systems. This result implicates that the friction between an ångstrom-scale buckled graphene layer and the second layer may be strongly enhanced in a local fashion relative to the friction between two non-buckled graphene layers. In summary, there are three factors that may counteract the deformation energy and thermal fluctuations, i.e., (1) the strong interactions between layers with local *AA* stacking, (2) the collective effect of van der Waals interactions, and (3) the increased friction between the buckled layer and the second layer. The three effects together may provide sufficient in-plane friction both in local areas and in the global structures to prevent the ångstrom-scale buckling structures from relaxing over time, thus stabilizing the ångstrom-scale buckling structure within the bilayer systems. Nevertheless, we are aware that further theoretical and experimental studies are necessary to fully establish these arguments, which is beyond the scope of this paper.

Second, let us deal with the question of *why the buckling chooses an ångstrom-scale wavelength instead of a mesoscopic wavelength*. This may be explained as a consequence of the dynamics of Euler buckling instability. When there is no other interaction interfering with the buckling, the buckling wavelength λ grows with time t via a coarsening process by a relationship of $\lambda(t) \sim t^{1/4}$ (Ref. 23 of the paper). (The coarsening of the buckling amplitude with time also follows the same mathematical form.) This means that the buckling begins with a wavelength as small as possible, but will slowly evolve to longer wavelengths. (If there is any buckling that happens on the ångstrom-scale in graphene, the wavelength can only have three options in terms of the number of unit cells of the graphene honeycomb lattice, i.e., 2, 3, and 4.) Interestingly, this theoretical standpoint plays a role in the proposed qualitative mechanism for buckling structure formation. During the course of solvent removal by vacuum drying, the recessive movement of the meniscus interface of the solvent sandwiched between two layers rapidly applies compressive strain to the local bulge area where the solvent has been removed. The local increase in compressive force is so rapid that the buckling instability takes place immediately at the site where solvent is removed, which also requires the buckling to first happen at the shortest possible length scale. At the same time, when the buckling begins, the meniscus interface of the sandwiched solvent brings the two opposite layers together with its interfacial tension, which allows the local inter-layer van der Waals interaction between the buckled side and the flat side to be formed within a time scale of t_v (Panel 4 in Supporting Fig. S4). The inter-layer interaction immediately stops the coarsening of the buckling wavelength. As long as the moving speed of the meniscus interface is fast enough to allow $t_v < t_n$, where t_n is the time scale of the λ coarsening from ångstrom-scale to nanoscale, the ångstrom-scale buckling structure will be fixed by the inter-layer interaction. Thus, the observation of ångstrom-scale buckling provides supporting evidence for the dynamic theory of the Euler buckling instability[23].

Let us turn back to the first question now. With the above argument in mind, the first question can be restated as: <u>*How does the buckling choose the smallest possible wavelength at a time $t < t_v$*</u>? Our calculation shows that the ε_c for a wavelength of two unit cells is much larger than that for three unit cells. In the case of graphene without folding behaviour, this means that choosing the wavelength of three unit cells results in a lower buckling energy. Indeed, when we performed DFT calculations without considering the boundary constraint of the folding behaviour, we found that the 2 × 3 array of unit cells, under the same strain observed for the 3.6-Å buckling structure, chooses to buckle in a wavelength of three unit cells at its ground energy (data not shown). Moreover, even if the wavelength of two unit cells is chosen at the beginning, the coarsening of the wavelength from two unit cells to three unit cells could be rapid enough to be completed in a time scale $t_a < t_v$ for a non-folded graphene layer, which results in the wavelength of three unit cells being fixed by inter-layer interactions. In the case of graphene with folding behaviour, choosing the wavelength of three unit cells is not compatible with the folding edge behaviour, because it causes higher folding energy at the folding edge. Instead, choosing the wavelength of two unit cells in the *x*-direction and three unit cells in the *y*-direction (the folding-line direction) would allow the sum of the buckling energy and the folding energy to be the lowest. Taken together, our analysis suggests that *at the very beginning* (when $t < t_v$)*, the liquid-phase-induced buckling chooses the smallest possible wavelength with the lowest total deformation energy in structural transformation that can be stabilized by the second layer*.

S5. Symmetry breaking and reduced dimensionality of buckling

The origin of the reduced dimensionality of the ångstrom-scale buckling structures may be attributed to symmetry breaking of the atomic structure upon the occurrence of the Euler buckling instability. The Euler buckling instability is a bifurcation phenomenon that is always accompanied by symmetry breaking[23]. The buckling in the *x*-direction on an ångstrom-scale wavelength substantially increases the bending modulus of the graphene sheets along the *y*-direction[24-27]. Energetically, ångstrom-scale buckling in two dimensions with the same amplitude and wavelength in both *x*- and *y*-dimensions incurs a much higher energy penalty than applies to buckling in one dimension; this high energy state cannot be balanced and stabilized by the inter-layer interactions. Indeed, we have performed DFT calculations under biaxial strains (0.09 in the both *x*- and *y*-directions), and observed that the 6.4-Å buckling structure spontaneously chooses a one-dimensional configuration that has the lowest deformation energy (Supporting Fig. S6). In other words, an ångstrom-scale buckling manifold with equal amplitudes in the both *x*- and *y*-directions is energetically unfavored and quite unstable. Our DFT calculations suggest that, without the boundary condition set by the folding edge, the 3.6-Å buckling structure will relax to the one-dimensional 6.4-Å buckling structure (data not shown), and that the 3.6-Å buckling structure can only stably exist around the folding line. Still, its unit manifold consisting of a 2 × 3 array of unit cells is a consequence of symmetry breaking.

Supplementary Figures

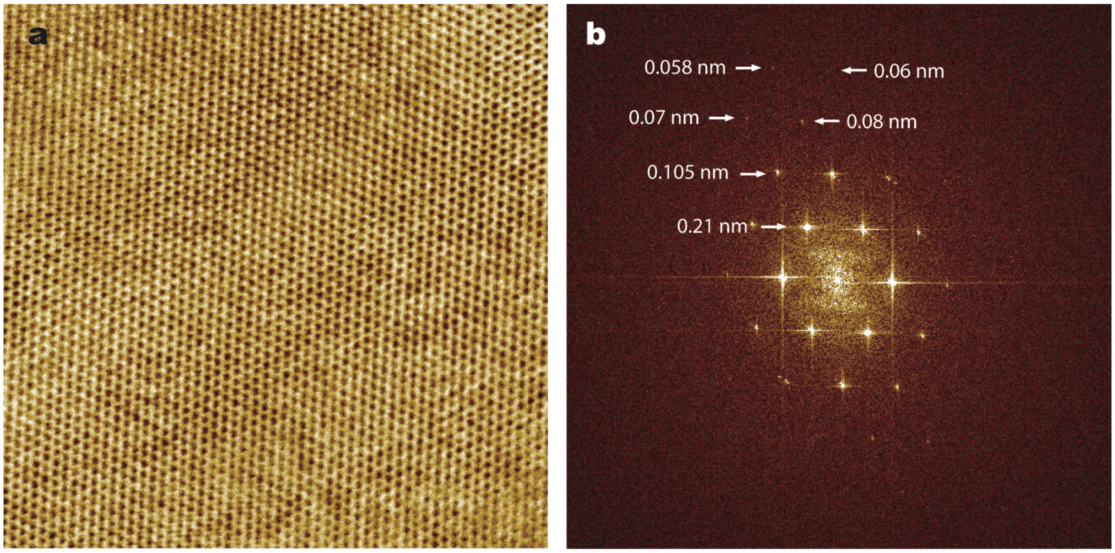

Supporting Figure S1. a, Typical monochromatised, aberration-corrected TEM image of a flat multilayer graphene area. **b,** the Fourier spectrum of **a** with spatial frequencies marked. The spatial frequency of 0.058 nm is clearly shown, demonstrating that the in-plane information limit of the microscope is well adjusted to 0.58 Å.

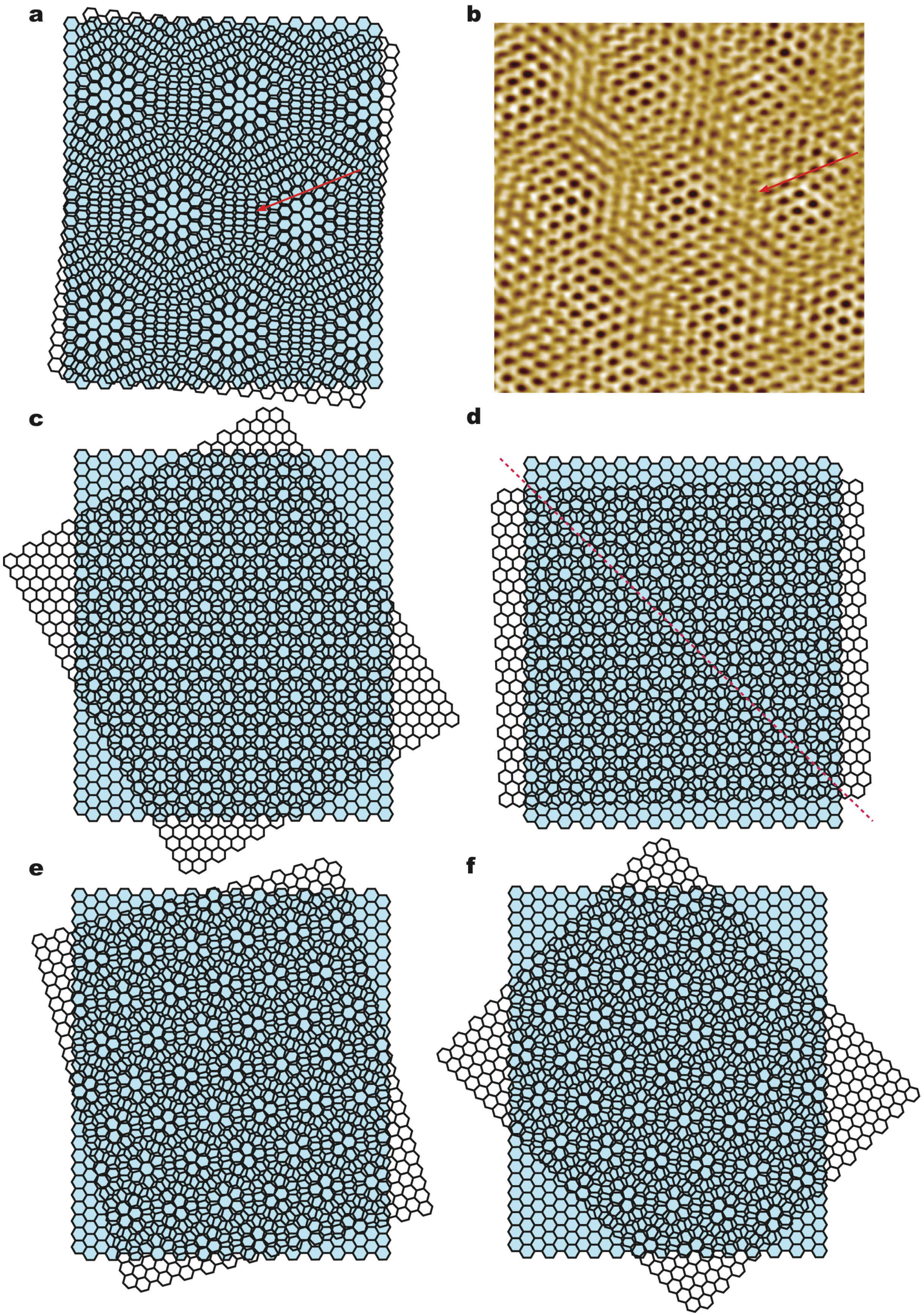
a
b
c
d
e
f

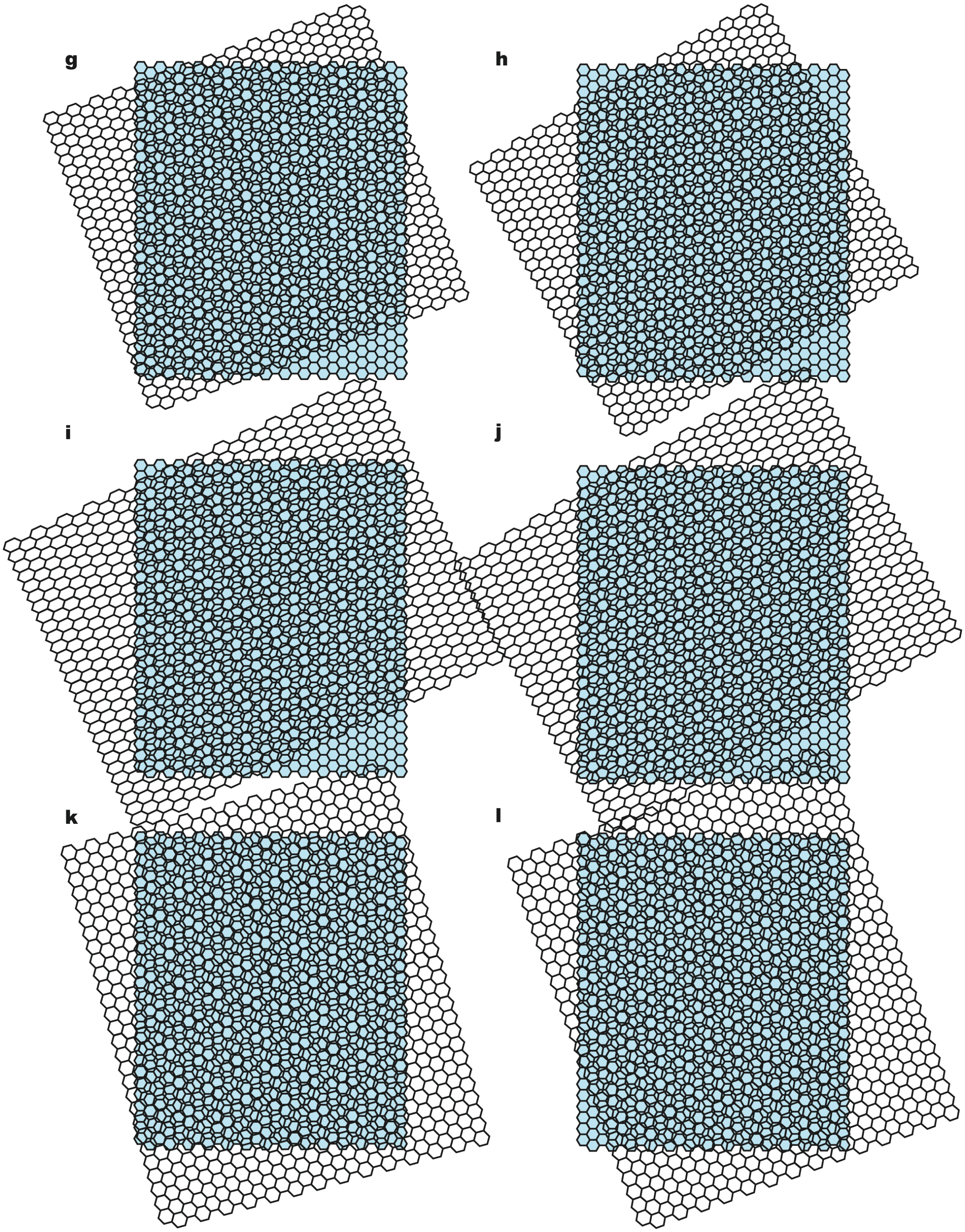

Supporting Figure S2. Moiré fringe patterns in graphene. **a**, Simulated moiré fringe pattern produced by two graphene monolayers that are overlaid at a small angle. **b**, Sub-ångstrom resolution TEM image of a moiré fringe pattern that reproduces the pattern shown in **a**. Red arrow indicates the local area that cannot be explained by the atomic model of a graphene monolayer, but can be well explained by an atomic model of two overlaid graphene layers (as indicated by the area in **a** marked by the red-arrow). A small ripple in graphene may give rise to the slight in-plane disorder in the pattern, as observed here. The good agreement between **a** and **b** shows that the simulated moiré fringe patterns are reliable and can be used as controls to determine whether certain TEM images are moiré fringe patterns. **c**, Simulated moiré fringe pattern produced by two monolayers that are overlaid at 30°, which is used as a control to compare with the TEM images of the 6.4-Å buckling structure, which has a 30° rotation of the two interacting graphene layers. The disagreement between the simulated pattern and the TEM images of the 6.4-Å buckling structure helps rule out the possibility that the TEM images are artifacts arising from moiré fringe. **d**, Simulated moiré fringe pattern produced by two monolayers that have mirror symmetry along the red dashed line, which is used to simulate the two opposite sides of a folded graphene monolayer. The direction of the red dashed line is equivalent to the experimentally observed folding-line direction. This is used as a control to compare with the TEM images of the 3.6-Å buckling structure. The disagreement between the simulated pattern and the TEM images of the 3.6-Å buckling structure helps rule out the possibility that the TEM images are artifacts arising from moiré fringe. **e**, Simulated moiré fringe pattern produced by two monolayers that are overlaid at 15°. **f**, Simulated moiré fringe pattern produced by two monolayers that are overlaid at 45°. **g** and **h**, Simulated moiré fringe patterns produced by one monolayer uniaxially elongated by a factor of 125% and overlaid at 20° and 30° over the other monolayer, respectively. **i** and **j**, Simulated moiré fringe patterns produced by one monolayer uniaxially elongated by a factor of 150% and overlaid at 25° and 30° over the other monolayer, respectively. **k** and **l**, Simulated moiré fringe patterns produced by one monolayer biaxially elongated by a factor of 125% and overlaid at 20° and 30° over the other monolayer, respectively. In **g**–**l**, we only show the overlaying angle that can produce the moiré patterns with wavelengths closest to 3.6 and 6.4 Å. They apparently cannot account for the TEM observations of the two buckling structures. We also simulated moiré fringe patterns produced by two monolayers that are overlaid at arbitrary angles, and by two monolayers with one layer biaxially (and uniaxially) elongated (and compressed) by a factor from 50% to 150% and overlaid by arbitrary angles against the other. None of them produce comparable patterns that can be directly used to explain the TEM images of the buckling structures (data not shown).

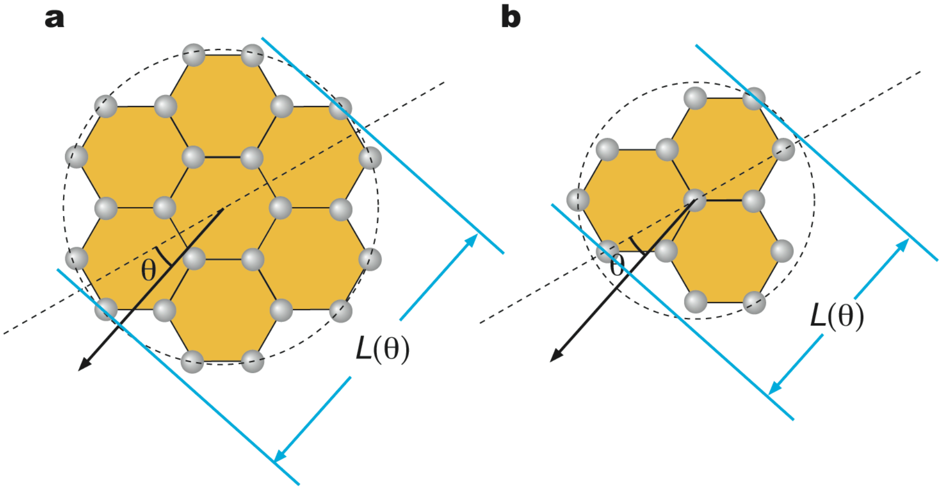

Supporting Figure S3. Schematics showing the configuration of the graphene ribbons used for the calculation of the critical strain $\varepsilon_c(\theta)$. **a,** The scheme used to calculate the ε_c for the onset of the 6.4-Å buckling formation. **b,** The scheme used to calculate the ε_c for the onset of the 3.6-Å buckling formation.

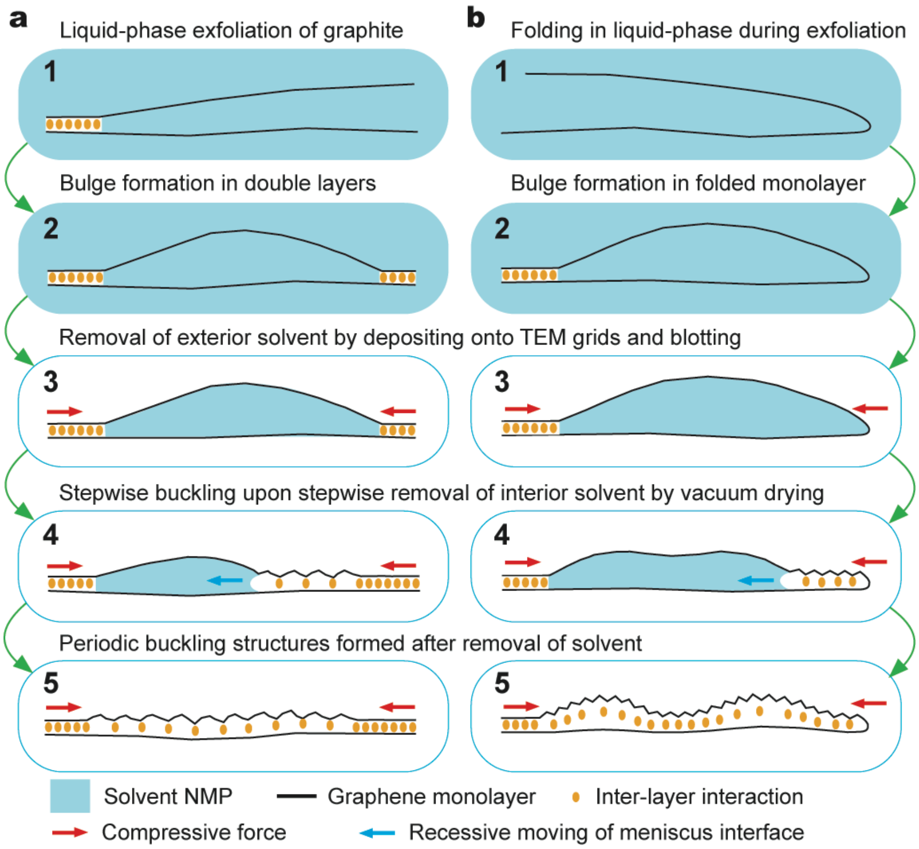

Supporting Figure S4. A possible mechanism for the formation of periodic buckling during liquid-phase processing of graphene. **a** and **b,** The schematics illustrating the possible mechanism for the formation of the 6.4-Å and 3.6-Å buckling structures, respectively. Panels **1** and **2**: (**a**) When two curved monolayers partially adhere by inter-layer interactions, the mismatch of the hexagonal lattice between different locally adhered regions may introduce bulge areas with solvent sandwiched in between the layers. (**b**) When one side of a folded monolayer is absorbed to its other side, a bulge area with sandwiched solvent may also be introduced in the vicinity of the folding edge. Panel **3**: The exterior solvent is removed by depositing the graphene dispersion onto TEM grids and blotting with filter papers. The in-plane static friction force in the locally adhered area prevents the graphene layers from sliding against each other and helps establish stress in the bulge area that may be balanced by the thermal pressure of the interior solvent. Panel **4**: When the vacuum drying drives the meniscus interface of the sandwiched solvent to move along the graphene surface, the curvature in the bulge area is transformed into in-plane compressive strain, which promotes stepwise buckling. This results in the buckling structures with ångstrom-scale wavelengths (Panel **5**).

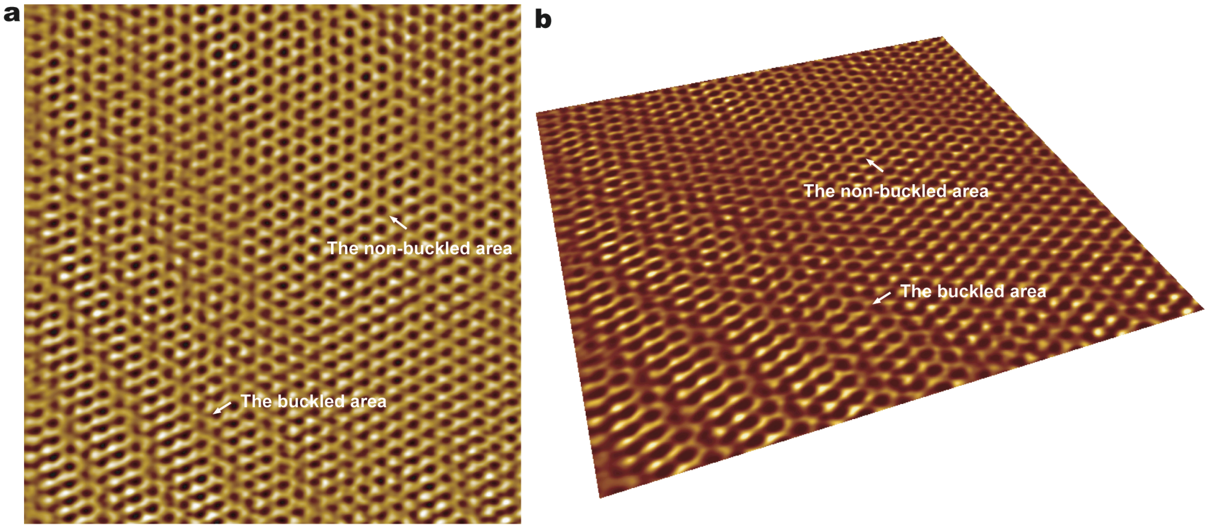

Supporting Figure S5. a, A TEM image showing the transition from a 6.4-Å buckled area to an area without ångstrom-scale buckling in the same monolayer. **b**, The 3D reconstruction of the perspective view of **a**.

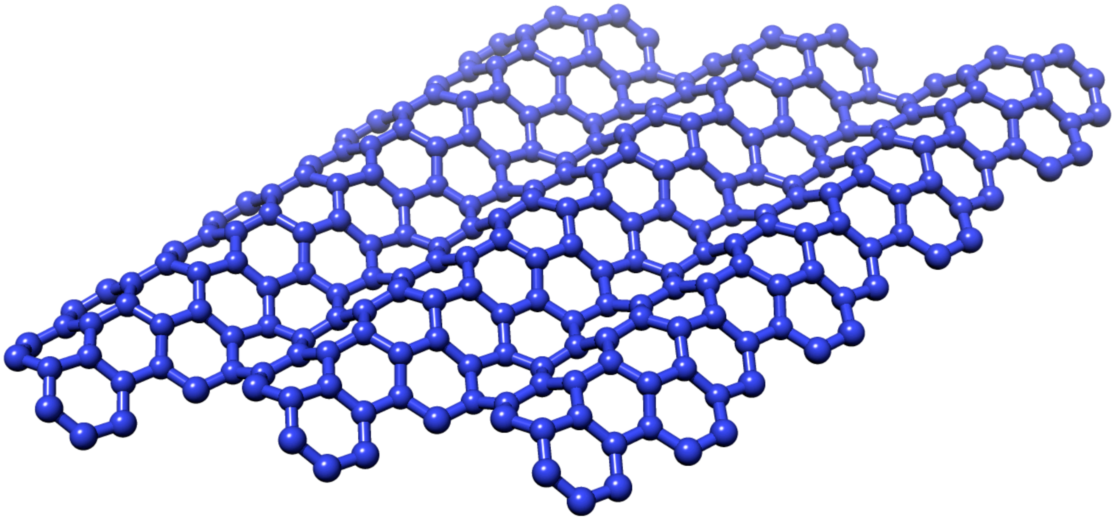

Supporting Figure S6. The reduced dimensionality of the 6.4-Å buckling structure under biaxial strains. The buckling structure shown is calculated by DFT, under the assumed strains of 0.09 in the both *x*- and *y*-directions. The DFT calculation is done to identify the atomic configuration with the lowest deformation energy under the given strains. The reduced dimensionality may be understood as a consequence of the buckling in the *x*-direction substantially increasing the bending modulus of graphene in the *y*-direction, thus making buckling with the same amplitude in both directions energetically unfavorable.

References

31. de Andres, P. L., Ramirez, R. & Verges, J. A. Strong covalent bonding between two graphene layers. *Phys. Rev. B* **77**, 045403 (2008).

32. Latil, S. & Henrard, L. Charge carriers in few-layer graphene films. *Phys. Rev. Lett.* **97**, 036803 (2006).

33. Gomez-Santos, G. Thermal van der Waals interaction between graphene layers. *Phys. Rev. B* **80**, 245424 (2009).

34. Dobson, J. F., White, A. & Rubio, A. Asymptotics of the dispersion interaction: analytic benchmarks for van der Waals energy functionals. *Phys. Rev. Lett.* **96**, 073201 (2006).

35. Horiuchi, S. et al. Carbon nanofilm with a new structure and property. *Jpn. J. Appl. Phys.* **42**, L1073-L1076 (2003).

36. Allinger, N. L. & Eaton, P. E. The geometries of pentaprismane and hexaprismane: insights from molecular mechanics. *Tetrahedron Lett*. **24**, 3697-3700 (1983).

37. Lee, C., *et al*. Frictional characteristics of atomically thin sheets. *Science* **328**, 76-80 (2010).